LETTERS

Fault-induced seismic anisotropy by hydration in subducting oceanic plates

Manuele Faccenda[1], Luigi Burlini[2], Taras V. Gerya[1] & David Mainprice[3]

The variation of elastic-wave velocities as a function of the direction of propagation through the Earth's interior is a widely documented phenomenon called seismic anisotropy. The geometry and amount of seismic anisotropy is generally estimated by measuring shear-wave splitting, which consists of determining the polarization direction of the fast shear-wave component and the time delay between the fast and slow, orthogonally polarized, waves. In subduction zones, the teleseismic fast shear-wave component is oriented generally parallel to the strike of the trench[1], although a few exceptions have been reported (Cascadia[2] and restricted areas of South America[3,4]). The interpretation of shear-wave splitting above subduction zones has been controversial and none of the inferred models seems to be sufficiently complete to explain the entire range of anisotropic patterns registered worldwide[1]. Here we show that the amount and the geometry of seismic anisotropies measured in the forearc regions of subduction zones strongly depend on the preferred orientation of hydrated faults in the subducting oceanic plate. The anisotropy originates from the crystallographic preferred orientation of highly anisotropic hydrous minerals (serpentine and talc) formed along steeply dipping faults and from the larger-scale vertical layering consisting of dry and hydrated crust–mantle sections whose spacing is several times smaller than teleseismic wavelengths. Fault orientations and estimated delay times are consistent with the observed shear-wave splitting patterns in most subduction zones.

Shear-wave splitting occurs when shear waves propagate in anisotropic elastic media. Strain-induced crystal preferred orientation (CPO) of anisotropic minerals is considered to be the main source of mantle anisotropy[5,6]. CPO is produced locally in faults in the plastic part of the lithosphere or, more extensively, in the viscous upper mantle, where anisotropic olivine grains align by dislocation creep[7,8]. Preferred orientation of faults, cracks, tabular intrusions and fine layering of two or more media with different elastic properties can produce an additional anisotropic mechanism (shape preferred orientation; SPO), provided that the spacing is smaller than the seismic wavelength to a sufficient degree[9,10].

Vertically travelling, long-period SKS waves, generated by the conversion of P waves at the core–mantle boundary, are often used to determine the anisotropy in subduction zones. Because the lower mantle is known to have no seismic anisotropy[8], SKS anisotropy in forearcs is commonly interpreted as being produced by trench-parallel flow of a dry upper mantle (A-type olivine, flow parallel to fast axis), both below and above the subducting slab[1], or by two-dimensional trench-normal flow of a hydrated[11] mantle wedge (B-type olivine, flow normal to fast axis). Despite the fact that considerable slab trench-parallel anisotropy was detected in some subduction zones (see, for example, ref. 12), the slab-induced splitting is normally assumed to be low and related to the trench-normal fossilized anisotropy of the downgoing lithosphere[1].

However, these interpretations are in contrast with the experimental observations and with part of the local S-wave splitting patterns. For example, analogue and numerical modelling of slab retreat indicates that the toroidal component of the mantle flow is oriented perpendicular to the slab, not parallel to it[13,14]. If we assume a dry mantle in which the A-type olivine fast axis is aligned parallel to the flow direction, it follows that the sub-slab-induced anisotropy must be oriented perpendicular to the trench and that the SKS anisotropic source(s) must lie within or above the slab. Mantle wedge-splitting measurements performed with local S waves show that the fast components can be oriented either parallel (constructive interference) or perpendicular (destructive interference) to that measured with SKS waves[1]. In addition, low splitting delay times of the mantle wedge (little or no interference) measured at the South America and Sumatra subduction zones suggest that the anisotropy sited above the slab can contribute only occasionally to the SKS splitting.

Where is the main source for SKS anisotropy located? A close inspection of the slab fabric can help us in answering this question. The subducting oceanic plate is pervasively affected by localized serpentinization. Faulting of the oceanic plate along trenches and along active and fossil volcanic ridges may form a dense network of preferentially oriented faults, providing a pathway for water percolation in the crust and the mantle[15–17]. Considerations about the triggering mechanism of earthquakes at intermediate depths nucleating in the lower plane of the Wadati–Bienoff zone place the hydration depth several tens of kilometres below the upper boundary of the slab[18,19]. Shallow seismicity and low heat flux measured at the trench slope also indicate that hydration continues at shallow depths[16,17,20].

To investigate how those sets of faults form and how their orientations change as the slab is subducted, we performed two-dimensional numerical experiments in which an oceanic plate bends spontaneously under the control of realistic visco-elasto-plastic rheologies (Supplementary Fig. 1; see Methods for details of the numerical model). The models show that when subduction is in a steady-state condition, faults dip at about 30° from the vertical at the trench, whereas below the forearc they attain a near-vertical orientation (Fig. 1). The results are consistent with the fault geometry of the outer rise and with focal-plane solutions of intermediate-depth earthquakes[16,21], as well as with the common 8–40-km thickness of double Benioff zones interpreted as sites of dehydration of subducted slabs[18,22]. Therefore, in the forearc region, where dehydration reactions have not yet affected the cold core of the slab and faults are near the vertical, a large-scale texture composed of low-velocity hydrated zones, including the faults and the adjacent wall rocks, and high-velocity areas of dry peridotite may both be present within the upper part of the descending plate.

Large faults spaced about 2.5 km apart and average degrees of serpentinization of the plate ranging from 17% to 25% have been

[1]Institute of Geophysics, ETH Zürich, Schafmattstrasse 30, 8093 Zürich, Switzerland. [2]Institute of Geology, ETH Zürich, Leonhardstrasse 19, 8092 Zürich, Switzerland. [3]Geosciences Montpellier, Université Montpellier II and CNRS, 34090 Montpellier, France.

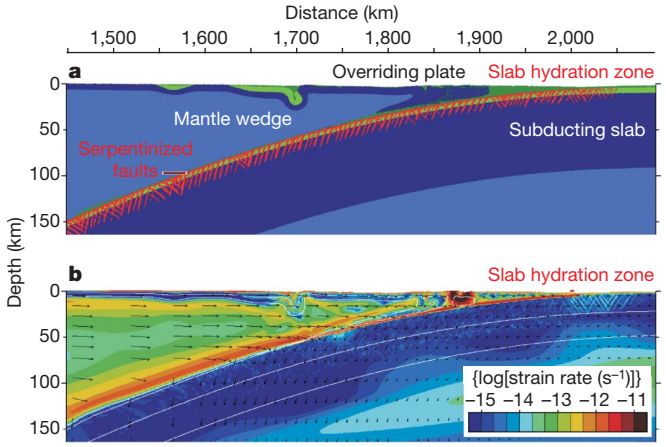

Figure 1 | Thermo-mechanical two-dimensional model of a spontaneously bending oceanic plate. **a**, Compositional map. Serpentinized faults are trenchward dipping but sets of antithetic and seaward-dipping faults are occasionally visible. Light green is gabbroic oceanic crust; basalt and sediments are shown in dark green. **b**, Strain rate map. Fault activation due to the bending of the plate occurs mainly at the trench in the upper layer of the slab. Arrows indicate the direction of material displacement. White lines are isotherms in °C (see Methods for details of the numerical model).

reported[17,23]. If we assume that hydration occurs mainly close to large faults, an upper oceanic plate section would be then formed by layers 400–600 m thick interbedded with dry portions of the mantle 1,900–2,100 m wide. Shear-wave splitting generated by preferentially oriented layers one order of magnitude thicker than the spacing of large outer-rise faults has already been reported[24]. Moreover, it has recently been shown that the long-wavelength SKS waves are indeed able to detect the anisotropy produced by bodies a few tens of kilometres thick (for example, the 10–20-km-thick shear zone of ref. 25; see also discussion in Supplementary Information). Hence, for vertically incident teleseismic waves, the slab can be considered to be a transverse isotropic body with a horizontal axis of symmetry.

Hydration of ultramafic rocks leads to the formation of sheet silicates such as lizardite, antigorite, talc and chlorite. Anisotropies of sheet silicates are highest for waves travelling in the (001) plane (up to 82% for lizardite), so that a near-vertical preferred orientation of hydrous minerals in the upper mantle will produce an important anisotropic source detectable by teleseismic waves. Microstructural analysis of serpentinized rocks deformed either naturally (see, for example, Supplementary Fig. 2) or in laboratory experiments indicate that the (001) plane of sheet silicates tends to align parallel to the shear zone during and after serpentinization[26,27], and that the CPO can be continuous along strike for as much as 50 km (ref. 28).

We propose a new model for the observed shear-wave splitting in the forearc, in which the resultant anisotropy is a combination of the SPO produced by near-vertical layers of rocks having different elastic properties and of the CPO of highly anisotropic hydrous minerals oriented parallel to the faults (Figs 2a, b and 3). The total amount and direction of the splitting would then be a function of the orientation, size, spacing and aspect ratio of the faults (Fig. 2c). The total delay time ($t_{d,tot}$) is

$$t_{d,tot} = t_{d,SPO} + t_{d,CPOhyd} \pm t_{d,CPOol}$$

where $t_{d,SPO}$ and $t_{d,CPOhyd}$ are the delay time contributions of the geometrical effect and the preferred alignment of hydrous minerals, respectively. Because the slab fossil anisotropy ($t_{d,CPOol}$) is perpendicular to magnetic lineations and spreading fabric trends that in most cases are oriented parallel to the trench at the outer rise (see, for example, ref. 15), the CPO of the olivine and enstatite grains will interfere constructively with that of the sheet silicates in faults at a high angle from the trench strike (CPO_{hyd+ol}; see Methods for details of the anisotropy model).

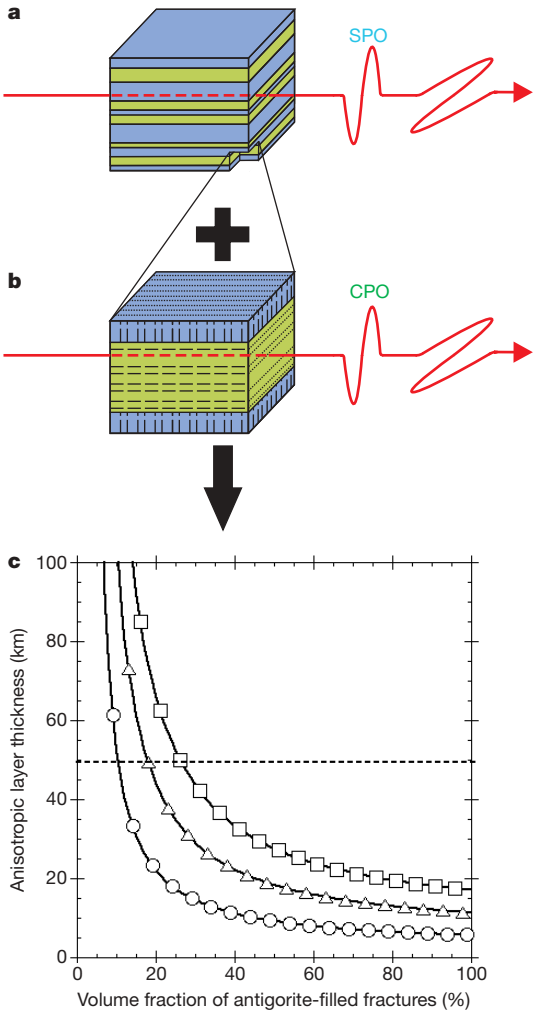

Figure 2 | Schematic diagram of the anisotropic components and estimates of the delay time. **a**, Thin layering of dry (blue) and hydrated (green) mantle portions results in an SPO-induced anisotropy for long-wavelength SKS waves. **b**, $CPO_{(hyd-ol)}$ formed by hydrated minerals parallel to the layering in the hydrated mantle and by perpendicular olivine and enstatite grains in the dry mantle (destructive interference). **c**, Contours of delay time for an anisotropic plate dipping at 30° with strong transverse isotropic antigorite, as a function of the volume fraction of antigorite-filled fractures and fault length, with a fracture aspect ratio of 100:1 (see Methods for details of the anisotropy model). Delay times: circles, 0.5 s; triangles, 1.0 s; squares, 1.5 s. The horizontal dashed line indicates a 50-km-thick antigorite layer.

Calculated delay times can account for more than 50% of those measured in the forearc (Table 1), indicating that slab anisotropy can indeed constitute the main anisotropic source of the upper mantle, provided that the faults extend deeply in the slab and the orientation is parallel to the fast splitting direction.

In most subduction regions, where vertical distances between the upper and lower planes of the double Benioff zone range from 10 to 50 km (refs 18, 22), bending-related faults trend parallel to the trench and to the direction of the fast shear-wave (SKS) component of the forearc (Fig. 4). We also found that in forearc regions where the fast shear-wave component is subparallel to the convergence direction, faults are at a high angle to the trench.

One of these cases is South America, where the fast components are generally oriented parallel to the trench. However in Central Chile, between 30° and 32° S, fast splitting directions are trench-normal, trending ENE[4], and seem to align roughly parallel with elongated clusters of intermediate-depth earthquakes coincident with the

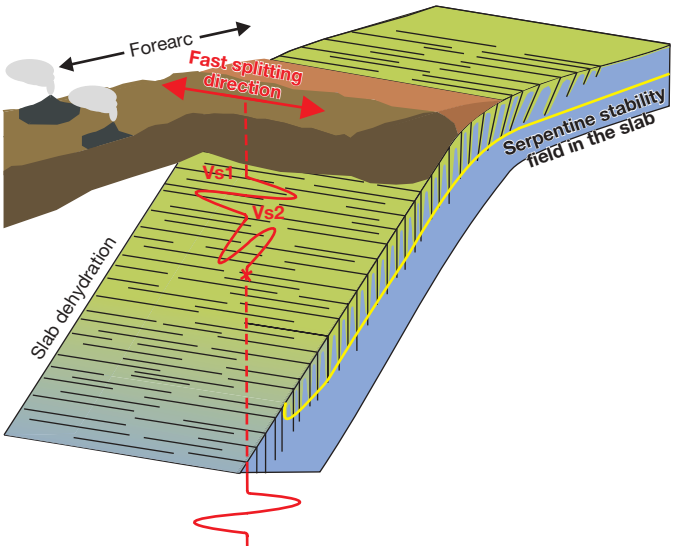

Figure 3 | Schematic diagram of the tectonic and compositional structure of the slab and the inferred splitting behaviour. Vs1 and Vs2 are the fast and slow, orthogonally polarized, shear waves, respectively. The polarization of Vs1 aligns parallel to the strike of the fault set. The colour scheme of the slab is as in Fig. 2a, b.

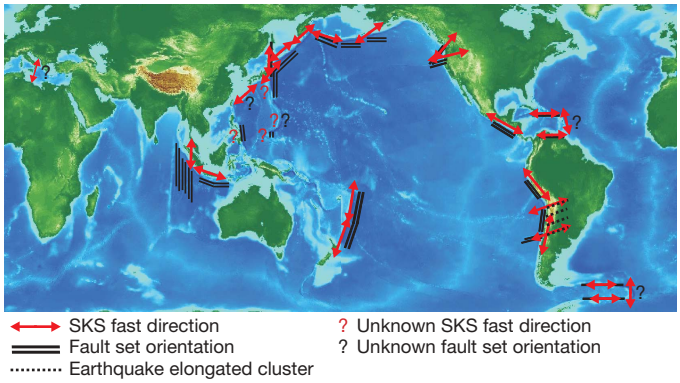

Figure 4 | Summary of SKS fast directions and fault set orientations. Question marks indicate that no data are available. See Methods for data sources.

projected continuation of the subducted Juan Fernández Ridge[16]. The nodal planes of these clusters have azimuths similar to those of trench faults flanking the offshore volcanoes of the Juan Fernández Ridge and penetrating as deep as 30 km in the lithosphere[16], suggesting that there might be a close relation between the orientation of the fault set, earthquake clusters and the anisotropic pattern. Further north, other ENE–NE-trending earthquake clusters that parallel trends in Cenozoic offshore volcanic chains have been identified (see Fig. 7 of ref. 29). These elongated clusters coincide with ENE–NE-trending, trench-normal splitting directions identified in ref. 3 in restricted areas of South America. Thus, subduction at a high angle from the trench of volcanic chains flanked by hydrated faults can explain occasional trench-normal splitting patterns such those observed in South America.

In Cascadia, although fractures trend NE–ENE[30], parallel to the SKS fast splitting directions[2], the fact that the Juan de Fuca plate is young and hot confines the slab hydration to shallow depths. Because anisotropies of the crust and of the mantle wedge are perpendicular to that measured with SKS waves, we believe that the main anisotropic source in Cascadia should lie in the below-slab mantle, an interpretation that is compatible with analogue and numerical models[13,14].

We note here that our anisotropy model and calculated time delays are intended as an upper-limit case in which sheet minerals are mostly aligned in the vertical direction parallel to fractures, whereas foliation at a high angle to the shear zone borders and isotropic microstructures have been recognized in serpentinites (see, for example, ref. 26). In addition, it has been shown[31] that the magnitude of shear-wave splitting often (but not always) decreases for ray paths at high angles to the foliation. Despite the uncertainties regarding the behaviour of serpentinite, hydrated portions of the slab with non-subvertical orientation of the foliation should contribute less to the CPO-induced anisotropy. In contrast, our calculations do not take into account the possibility that water could remain trapped inside fractures with sealing serpentinized margins. A preferential orientation of subvertical water-filled cracks at a high pore pressure could constitute an additional anisotropic source (SPO[10]) and further increase the estimated shear-wave-splitting delay time (N. I. Christensen, personal communication; see Methods and Supplementary Fig. 4). Indeed, we believe that the slab anisotropy is a combination of CPO, SPO and fluid-filled cracks.

From our calculations of anisotropy, our numerical model of slab-bending-related faults and observations including trench bathymetry[17], slab anisotropy measurements[12], SKS splitting patterns[1] and earthquake distributions[16,29], we conclude that in subduction zones SKS splitting seems to be related more to the spatial distribution of the slab faulting than to the flow in the upper mantle. The magnitude of the splitting produced by localized hydration of the oceanic plate (Fig. 2) depends mainly on the fault depth and on the degree of hydration of the slab. In a young and hot slab (that is, shallow faults), the calculated amount of delay time can be lower (Table 1) than those measured, indicating that further sources in the upper mantle are needed. As discussed above, analogue and numerical models show that the below-slab mantle can contribute to the observed anisotropy only when the splitting patterns are trench-normal (for example, Cascadia). In contrast, a hydrated mantle wedge dominated by two-dimensional corner flow and composed of B-type olivine and subvertical hydrous minerals[32] would be a good candidate for this additional anisotropic layer. We suggest that the main anisotropic sources of SKS waves lie within the slab, with additional contributions coming from the mantle wedge if the local S-wave anisotropy is oriented parallel to that of SKS waves.

Table 1 | Shear-wave-splitting delay times

Fracture aspect ratio	Fault length (km)				
	10	20	30	40	50
1:5	0.26	0.51	0.77	1.03	1.29
1:100	0.35	0.71	1.06	1.41	1.77

For the differential effective medium (DEM) model, delay times (in seconds) are shown for vertically propagating S waves in an anisotropic plate dipping at 30° containing 30% by volume of vertical fractures filled with oriented antigorite. The subvertical factures have propagated to different depths into the plate from the plate's top surface. See Methods for details of the anisotropy model.

METHODS SUMMARY

The employed numerical technique is based on a combination of a finite difference method, applied on a staggered irregular grid, and a marker-in-cell technique. The momentum, continuity and energy equations are solved on the Eulerian frame, and physical properties are transported by Lagrangian markers that move according to the velocity field interpolated from the fix grid. Realistic and non-Newtonian visco-elasto-plastic rheologies are used in the model (Supplementary Table 1). Subduction of oceanic plates is spontaneous and no velocity field is applied.

Splitting delay times were calculated with an averaged elastic tensor of dry peridotitic rocks and elastic properties of a serpentinized and foliated sample. Calculations were made for a 30° dipping slab with subvertical fractures of different aspect ratios; they include the combined effect of the SPO and CPO. We also undertook an upper-bound calculation of water-filled cracks (no antigorite present) in our anisotropic elastic model with a plate dipping at 30° using the properties of water at *in situ* conditions at 50 km depth (see Methods).

Full Methods and any associated references are available in the online version of the paper at www.nature.com/nature.

Received 28 April; accepted 27 August 2008.

1. Long, M. D. & Silver, P. The subduction zone flow field from seismic anisotropy: a global view. *Science* **319,** 315–318 (2008).
2. Currie, C. A., Cassidy, J. F., Hyndman, R. D. & Bostock, M. G. Shear wave anisotropy beneath the Cascadia subduction zone and western North American craton. *Geophys. J. Int.* **157,** 341–353 (2004).
3. Russo, R. M. & Silver, P. G. Trench-parallel flow beneath the Nazca plate from seismic anisotropy. *Science* **263,** 1105–1111 (1994).
4. Anderson, M. L., Zandt, G., Triep, E., Fouch, M. & Beck, S. Anisotropy and mantle flow in the Chile–Argentina subduction zone. *Geophys. Res. Lett.* **31,** L23608, doi:10.1029/2004GL020906 (2004).
5. Savage, M. K. Seismic anisotropy and mantle deformation: what have we learned from shear wave splitting? *Rev. Geophys.* **37,** 65–106 (1999).
6. Park, J. & Levin, V. Seismic anisotropy: tracing plate dynamics in the mantle. *Science* **296,** 485–489 (2002).
7. Nicolas, A. & Christensen, N. I. in *Composition, Structure and Dynamics of the Lithosphere–Asthenosphere System* (eds Fuchs, K. & Froidevaux, C.) 111–123 (Am. Geophys. Union, 1987).
8. Visser, K., Trampert, J., Lebedev, S. & Kennett, B. L. N. Probability of radial anisotropy in the deep mantle. *Earth Planet. Sci. Lett.* **270,** 241–250 (2008).
9. Backus, G. E. Long-wave elastic anisotropy produced by horizontal layering. *J. Geophys. Res.* **67,** 4427–4440 (1962).
10. Crampin, S. The fracture criticality of crustal rocks. *Geophys. J. Int.* **118,** 428–438 (1994).
11. Kneller, E. A., van Keken, E., Karato, S. & Park, J. B-type olivine fabric in the mantle wedge: insight from high-resolution non-Newtonian subduction zone models. *Earth Planet. Sci. Lett.* **237,** 781–797 (2005).
12. Matcham, I., Savage, M. K. & Gledhill, K. R. Distribution of seismic anisotropy in the subduction zone beneath the Wellington region, New Zealand. *Geophys. J. Int.* **140,** 1–10 (2000).
13. Kincaid, C. & Griffiths, R. W. Laboratory models of the thermal evolution of the mantle during rollback subduction. *Nature* **425,** 58–62 (2003).
14. Piromallo, C., Becker, T. W., Funiciello, F. & Faccenna, C. Three-dimensional instantaneous mantle flow induced by subduction. *Geophys. Res. Lett.* **33,** L08304, doi:10.1029/2005GL025390 (2006).
15. Masson, D. G. Fault patterns at outer trench walls. *Mar. Geophys. Res.* **13,** 209–225 (1991).
16. Ranero, C. R., Villaseñor, A., Phipps Morgan, J. & Weinribe, W. Relationship between bend-faulting at trenches and intermediate-depth seismicity. *Geochem. Geophys. Geosyst.* **6,** Q12002, doi:10.1029/2005GC000997 (2005).
17. Ranero, C. R., Phipps Morgan, J. & Reichert, C. Bending-related faulting and mantle serpentinization at the Middle America trench. *Nature* **425,** 367–373 (2003).
18. Peacock, S. M. Are the lower planes of double seismic zones caused by serpentine dehydration in subducting oceanic mantle? *Geology* **29,** 299–302 (2001).
19. Omori, S., Komabayashi, T. & Maruyama, S. Dehydration and earthquakes in the subducting slab: empirical link in intermediate and deep seismic zones. *Phys. Earth. Planet. Inter.* **146,** 297–311 (2004).
20. MacDonald, H. & Fyfe, W. S. Rate of serpentinization in seafloor environments. *Tectonophysics* **116,** 123–135 (1985).
21. Jiao, W., Silver, P. G., Fei, Y. & Prewitt, T. Do intermediate- and deep-focus earthquakes occur on preexisting weak zones? An examination of Tonga subduction zone. *J. Geophys. Res.* **105,** 28,125–28,138 (2000).
22. Brudzinski, M. R., Thurber, C. H., Hacker, B. R. & Engdahl, E. R. Global prevalence of double Benioff zones. *Science* **316,** 1472–1474 (2007).
23. Grevemeyer, I., Ranero, C. R., Flueh, E. R., Klaeschen, D. & Bialas, J. Passive and active seismological study of bending-related faulting and mantle serpentinization at the Middle America trench. *Earth Planet. Sci. Lett.* **258,** 528–542 (2007).
24. Gee, L. S. & Jordan, T. H. Polarization anisotropy and fine-scale structure of the Eurasian upper mantle. *Geophys. Res. Lett.* **15,** 824–827 (1988).
25. Babuska, V., Plomerova, J., Vecsey, L., Granet, M. & Achauer, U. Seismic anisotropy of the French Massif and predisposition of Cenozoic rifting and volcanism by Variscan suture hidden in the mantle lithosphere. *Tectonics* **21,** 1029, doi:10129/2001TC901035 (2002).
26. Norrel, G. T., Teixell, A. & Harper, G. D. Microstructure of serpentine mylonites from the Josephine ophiolites and serpentinization in retrogressive shear zones, California. *Geol. Soc. Am. Bull.* **101,** 673–682 (1989).
27. Escartin, J., Hirth, G. & Evans, B. Nondilatant brittle deformation of serpentinites: implications for Mohr–Coulomb theory and the strength of faults. *J. Geophys. Res.* **102,** 2897–2913 (1997).
28. Hirauchi, K. Serpentinite textural evolution related to tectonically controlled solid-state intrusion along the Kurosegawa Belt, northwestern Kanto Mountains, central Japan. *I. Arc* **15,** 156–164 (2006).
29. Kirby, S., Engdahl, R. & Denlinger, R. Intermediate-depth intraslab earthquakes and arc volcanism as physical expression of crustal and uppermost mantle metamorphism in subducting slabs. *Geophys. Monogr.* **96,** 195–214 (1996).
30. Chaytor, J. D. & Goldfinger, C. Dziak, R.P. & Fox, C. G. Active deformation of the Gorda plate: constraining deformation models with new geophysical data. *Geology* **32,** 353–356 (2004).
31. Okaya, D. A. & Christensen, N. I. Anisotropic effects of non-axial seismic wave propagation in foliated crustal rocks. *Geophys. Res. Lett.* **29,** 1507, doi:10.1029/2001GL014285 (2002).
32. Kneller, E. A., Long, M. D. & van Keken, P. E. Olivine fabric transition and shear wave anisotropy in the Ryukyu subduction system. *Earth Planet. Sci. Lett.* **268,** 268–282 (2008).

Supplementary Information is linked to the online version of the paper at www.nature.com/nature.

Acknowledgements We thank M. Savage and N.I. Christensen for critical discussion, reading of the manuscript and English polishing, and Gabriele Morra and F. J. Simons helping to improve the manuscript. L.B. thanks W. Weder for his work. This work was supported by ETH Research Grant TH-12/05-3 and SNF Research Grant 200021-113672/1.

Author Information Reprints and permissions information is available at www.nature.com/reprints. Correspondence and requests for materials should be addressed to M.F. (faccenda@erdw.ethz.ch).

METHODS

Numerical model. The numerical experiment was performed with I2ELVIS code developed by ref. 33. The computational domain is 3,000 × 200 km (1,001 × 141 nodes, ~5 million markers). Horizontal resolution moves together with the retreating slab and is maximal (1 km) starting 400 km on the right of the trench to 300 km on its left; elsewhere, the resolution increases gradually from 1 km to 20 km. Vertical resolution is 1 km for the first 80 km and 2 km for the last 120 km. The initial setup is shown in Supplementary Fig. 1. Subduction starts spontaneously[34] as the result of the juxtaposition of two plates of different ages (1 and 70 Myr for the left and right plates, respectively) along a transform fault that is assumed to be weak due to water percolation and hydration of the boundary (low plastic strength of 1 MPa; refs 34, 35). The thermal structure of the initial plate setup is computed according to the cooling of a semi-infinite half-space equation[36]:

$$T = T_1 + (T_0 - T_1)(1 - \mathrm{erf}(\eta))$$

$$\eta = d/2\sqrt{\kappa\tau}$$

where $T_0 = 0\,^{\circ}\mathrm{C}$ for both plates, $T_1 = 1{,}270$ and $1{,}350\,^{\circ}\mathrm{C}$ for the young and old plates, respectively, d is depth, κ is thermal diffusivity ($10^{-6}\,\mathrm{m^2\,s^{-1}}$), τ is the age in seconds of the plates and η is the dimensionless similarity variable. The age of the older plate decreases linearly towards the right boundary corresponding to a mid-ocean ridge (0 Myr). Serpentinization (that is, weakening) of the oceanic slab is assumed along the faults having a finite plastic strain of more than 0.01. A low-viscosity lower boundary (10^{19} Pa s, from 180 to 200 km depth) is imposed to facilitate slab penetration.

Anisotropic model. The composition of the plate is 70% olivine and 30% enstatite, where the plate is elastically anisotropic, calculated with the CPO from a database (refs 37, 38) of 110 and 68 samples for olivine and enstatite, respectively. The elastic tensors for olivine and enstatite were calculated at 500 °C and 1.5 GPa, corresponding to a depth of about 50 km on a warm slab geotherm[39]. For olivine we used the single crystal elastic constants and pressure derivatives reported in ref. 40 and the temperature derivatives in ref. 41. For enstatite we used the elastic constants and pressure derivatives in ref. 42 and temperatures derivatives in ref. 43. For antigorite we used the single crystal elastic constants determined recently through atomic modelling in ref. 44 under ambient conditions.

For the CPO inside serpentinized fractures, we used seismic velocities of naturally deformed antigorite measured in ref. 45 (see more details in Supplementary Fig. 3). The velocity measurements[45] show a transverse isotropic symmetry with velocities in the x and y directions for P and S waves being equal within experimental uncertainty, pressure-independent S-wave anisotropy, volumetric compaction of 1.2% and ratio of compaction strains between z and x or y of about 4:1. The compaction data would, to first order, constrain the fracture porosity to be about 1% and the aspect ratio to 4:1.

To obtain the CPO for antigorite, we used the March strain model[46], often used for characterizing (001) pole figures of naturally deformed layered silicates (see, for example, ref. 47). To produce an axial (001) pole figure similar to that reported in ref. 45 for a naturally deformed antigorite sample, we applied a series of axial strains with the March model to an initially uniform pole figure. To obtain the complete CPO we assumed that the crystallographic axes normal to the c axes were randomly distributed, which results in transverse isotropic (TI) elastic symmetry when combined with the elastic constants of antigorite. We increased the axial strain until the calculated velocities matched the experimentally measured velocity anisotropy reported in ref. 45.

The 21 elastic constants for the anisotropic plate (70% olivine, 30% enstatite) and 5 independent transverse isotropic elastic constants of the antigorite fracture fill represent the two elastic tensors of the end-member compositions in our model (Supplementary Table 2). We used the differential effective medium (DEM) to represent a two-phase composite model of the fractured plate by incrementally adding three-dimensional ellipsoidal inclusions of serpentine fracture fill to the anisotropic plate and then recalculating the new effective background material at each increment. The tensorial equations for the DEM model were derived in ref. 48 as

$$\frac{\mathrm{d}C_{\mathrm{DEM}}}{\mathrm{d}V} = \frac{1}{(1-V)}(C_i - C_{\mathrm{DEM}})A_i$$

where the term $A_i = [I + G(C_i - C_{\mathrm{DEM}})]^{-1}$ is the strain concentration factor coming from the Eshelby formulation of the inclusion problem, I being the unit elastic tensor, G the symmetrical tensor of Green's function, C_i the elastic constant of the serpentine fracture fill and C_{DEM} the elastic constant of the background material (that is, the plate) (see ref. 49 for more details and references). The ellipsoidal penny-shaped fractures had axial ratios along the x:y:z orthogonal directions of 1:5:5 to 1:100:100, where x is the horizontal axis normal to the subduction trench, y is parallel to the trench axis and z is the vertical axis. In our models, as a result of the very high anisotropy of TI antigorite, the fracture axial ratios of the fractures have little relative influence on shear-wave anisotropy (Supplementary Fig. 3).

To evaluate the possible contribution of penny-shaped cracks in the foliation inferred from the v_P velocity measurements of ref. 45, we have modelled the water-filled vertical fractures in the anisotropic plate. The calculated S-wave anisotropy is very high even for 5% of water-filled fractures (5–80%), depending very strongly on aspect ratio (Supplementary Fig. 4). Hence a small percentage of aligned water-filled cracks in the foliation plane will greatly enhance the anisotropy of a serpentine-filled fracture, even if the filling is isotropic. Because dry microcracks may be preserved and influence seismic properties to pressures as high as 1 GPa (ref. 50), fluid-filled cracks will be even more resistant to closure at high pressure.

Splitting and fault set pattern data. All the compiled data included in Fig. 4 regarding the worldwide orientations of SKS fast components and fault sets, and earthquake clusters located in South America were taken from the literature. SKS fast directions data are from refs 1–4, 51–53. Fault set orientation are from refs 15–17, 54–60. Earthquake elongated clusters are from ref. 29.

33. Gerya, T. V. & Yuen, D. A. Robust characteristic method for modeling multiphase visco-elasto-plastic thermo-mechanical problems. *Phys. Earth Planet. Inter.* **163,** 83–105 (2007).
34. Hall, C. E., Gurnis, M., Sdrolias, M., Lavier, L. L. & Muller, R. D. Catastrophic initiation of subduction following forced convergence across fractures zones. *Earth Planet. Sci. Lett.* **212,** 15–30 (2003).
35. Gerya, T. V., Connolly, J. A. D. & Yuen, D. A. Why is terrestrial subduction one-sided? *Geology* **36,** 43–46 (2008).
36. Turcotte, D. L. & Schubert, G. *Geodynamics* (Cambridge Univ. Press, 2002).
37. Ben Ismaïl, W. & Mainprice, D. A statistical view of the strength of seismic anisotropy in the upper mantle based on petrofabric studies of ophiolite and xenolith samples. *Tectonophysics* **296,** 145–157 (1998).
38. Ben Ismaïl, W. & Mainprice, D. An assessment of the contribution of enstatite to the upper mantle seismic anisotropy. *Tectonophysics*. (submitted).
39. Wada, I., Wang, K., He, J. & Hyndman, R. D. Weakening of the subduction interface and its effects on surface heat flow, slab dehydration, and mantle wedge serpentinization. *J. Geophys. Res.* **113,** B04402, doi:10.1029/2007JB005190 (2008).
40. Abramson, E. H., Brown, J. M., Slutsky, L. J. & Zaug, J. The elastic constants of San Carlos olivine to 17 GPa. *J. Geophys. Res.* **102,** 12253–12263 (1997).
41. Isaak, D. G. High-temperature elasticity of iron-bearing olivine. *J. Geophys. Res.* **97,** 1871–1885 (1992).
42. Chai, M., Brown, J. M. & Slutsky, L. J. The elastic constants of an aluminous orthopyroxene to 12.5 GPa. *J. Geophys. Res.* **102,** 14779–14785 (1977).
43. Jackson, J. M., Sinogeikin, S. V. & Bass, J. D. Sound velocities and single-crystal elasticity of orthoenstatite to 1073K at ambient pressure. *Phys. Earth Planet. Inter.* **161,** 1–12 (2007).
44. Pellenq R. J.-M. . *et al.* Atomistic calculations of the elastic properties of antigorite at upper mantle conditions: application to the seismic properties in subduction zones. *Earth Planet. Sci. Lett.*. (submitted).
45. Kern, H., Liu, B. & Popp, B. Relationship between anisotropy of P and S wave velocities and anisotropy of attenuation in serpentinite and amphibolite. *J. Geophys. Res.* **102,** 3051–3065 (1997).
46. March, A. Mathematische Theorie der Regelung nach der Korngestalt bei affiner Deformation. *Z. Kristallogr.* **81,** 285–297 (1932).
47. Paterson, S. R., Yu, H. & Oertel, G. Primary and tectonic fabric intensities in mudrocks. *Tectonophysics* **247,** 105–119 (1995).
48. McLaughlin, R. A. A study of the differential scheme for composite materials. *Int. J. Eng. Sci.* **15,** 237–244 (1977).
49. Mainprice, D. Modelling the anisotropic seismic properties of partially molten rocks found at Mid-Ocean. *Tectonophysics* **279,** 161–179 (1997).
50. Christensen, N. I. Compressional wave velocities in possible mantle rocks to pressures of 30 kilobars. *J. Geophys. Res.* **79,** 407–412 (1974).
51. Müller, C. Upper mantle seismic anisotropy beneath Antarctica and the Scotia Sea region. *Geophys. J. Int.* **147,** 105–122 (2001).
52. Russo, R. M. S. i. l. v. e. r. P. G. F. r. a. n. k. e. M., Ambeh, W. B. & James, D. E. Shear-wave splitting in northeast Venezuela, Trinidad, and the eastern Caribbean. *Phys. Earth Planet. Inter.* **95,** 251–275 (1996).
53. Müller, C., Bayer, B., Eckstaller, A. & Miller, H. Mantle flow in the South Sandwich subduction environment from source-side shear wave splitting. *Geophys. Res. Lett.* **35,** L03301, doi:10.1029/2007GL032411 (2008).
54. Chaytor, J. D., Goldfinger, C., Dziak, R. P. & Fox, C. G. Active deformation of the Gorda plate: constraining deformation models with new geophysical data. *Geology* **32,** 353–356 (2004).
55. Deplus, C. *et al.* Direct evidence of active deformation in the eastern Indian oceanic plate. *Geology* **26,** 131–134 (1998).
56. Lallemand, S. E. *et al.* Genetic relations between the central and southern Philippine trench and Sangihe trench. *J. Geophys. Res.* **103,** 933–950 (1998).
57. Masson, D. G. *et al.* Subduction of seamounts at the Java trench: a view with long-range sidescan sonar. *Tectonophysics* **185,** 51–65 (1990).
58. Billen, M. I. Seafloor morphology of the Osbourn Trough and Kermadec Trench. http://resolver.caltech.edu/CaltechETD:etd-11012001-142941 (2001).
59. Fujiwara, T. *et al.* Morphology and tectonics of the Yap trench. *Mar. Geophys. Res.* **21,** 69–86 (2000).
60. Kobayashi, K., Nakanishi, M., Tamaki, K. & Ogawa, Y. Outer slope faulting associated with the western Kuril and Japan trenches. *Geophys. J. Int.* **134,** 356–372 (1998).